Mueller matrix optical and magneto-optical characterization of Bi-substituted gadolinium iron garnet for application in magnetoplasmonic structures

L. Halagačka,[1,2*] K. Postava,[1] M. Vanwolleghem,[3] F. Vaurette,[3] J. Ben Youssef,[4] B. Dagens,[2] and J. Pištora[1]

[1]*Department of Physics and Nanotechnology Centre, Technical University of Ostrava, 17. listopadu 15, 708 33 Ostrava–Poruba, Czech Republic*

[2]*Institut d'Electronique Fondamentale, UMR CNRS 8622, Université Paris-Sud XI, Orsay, France*

[3]*Institut d'Electronique, Microelectronique et Nanotechnologie, CNRS UMR 8520, Villeneuve-d'Ascq, France*

[4]*Laboratoire de Magntisme de Bretagne, Université de Bretagne Occidentale , EA 4522/CNRS, Brest, France*

[*]*lukas.halagacka@gmail.com*

Abstract: A ferromagnetic garnet, used as a magneto-optical (MO) material in magneto-photonic and magneto-plasmonic structures, is characterized. We present a general procedure to determine optical and magneto-optical functions of the magneto-optic garnet by using Mueller matrix ellipsometry. In the first step, the optical functions (the refractive index spectra) of the (CaMgZr)-doped gallium-gadolinium garnet (sGGG) substrate and the Bi-substituted gadolinium iron garnet $Gd_{1.24}Pr_{0.48}Bi_{1.01}Lu_{0.27}Fe_{4.38}Al_{0.6}O_{12}$ (Bi:GIG) are obtained in the spectral range from 0.73 eV to 6.42 eV (wavelength range 193 nm – 1.7 μm). Subsequently, the spectra of the magneto-optical tensor components are obtained by applying an external in-plane magnetic field in longitudinal and transverse geometry. The obtained functions are then used to fit the Mueller matrix spectra of a magneto-plasmonic structure with a gold grating on the magneto-optic garnet layer. This structure has recently been demonstrated to have strongly enhanced transverse magneto-optic Kerr response at visible and near-infrared frequencies. By taking possible fabrication imperfections (surface roughness, residual photo-resist layer, thickness deviation) into account, the measured strongly enhanced MO response fits very well to the numerical model predicting these exaltations.

OCIS codes: (250.5403) Magneto-optic systems; (160.3820) Magneto-optical materials; (120.2130) Ellipsometry and polarimetry.

References and links

1. P. Hansen and J.-P. Krumme, "Magnetic and magneto-optical properties of garnet films," Thin Solid Films **114**, 69 – 107 (1984). Special Issue on Magnetic Garnet Films.

#215021 - $15.00 USD Received 1 Jul 2014; revised 30 Jul 2014; accepted 30 Jul 2014; published 22 Aug 2014

2. W. Śmigaj, J. Romero-Vivas, B. Gralak, L. Magdenko, B. Dagens, and M. Vanwolleghem, "Magneto-optical circulator designed for operation in a uniform external magnetic field," Opt. Lett. **35**, 568–570 (2010).
3. W. Śmigaj, L. Magdenko, J. Romero-Vivas, S. Guenneau, B. Dagens, B. Gralak, and M. Vanwolleghem, "Compact optical circulator based on a uniformly magnetized ring cavity," Phot. Nanostruct. - Fundam. Appl. **10**, 83 – 101 (2012).
4. H. Yokoi, T. Mizumoto, N. S. N. Futakuchi, and Y. Nakano, "Demonstration of an optical isolator with a semiconductor guiding layer that was obtained by use of a nonreciprocal phase shift," Appl. Opt. **39**, 6158–6164 (2000).
5. Y. Shoji, T. Mizumoto, H. Yokoi, I.-W. Hsieh, and R. M. Osgood, "Magneto-optical isolator with silicon waveguides fabricated by direct bonding," Appl. Phys. Lett. **92**, 071117 (2008).
6. M. C. Tien, T. Mizumoto, P. Pintus, H. Kromer, and J. E. Bowers, "Silicon ring isolators with bonded nonreciprocal magneto-optic garnets." Opt. Express **19**, 11740–5 (2011).
7. J. Fujita, M. Levy, R. M. Osgood, Jr., L. Wilkens, and H. Dötsch, "Waveguide optical isolator based on Mach-Zehnder interferometer," Appl. Phys. Lett. **76**, 2158–2160 (2000).
8. T. Izuhara, J. Fujita, M. Levy, and R. M. Osgood, Jr., "Integration of magnetooptical waveguides onto a III-V semiconductor surface," IEEE Phot. Technol. Lett. **14**, 167–169 (2002).
9. L. Bi, J. Hu, P. Jiang, D. H. Kim, G. F. Dionne, L. C. Kimerling, and C. A. Ross, "On-chip optical isolation in monolithically integrated non-reciprocal optical resonators," Nature Photonics p. 758?62 (2011).
10. V. Temnov, "Ultrafast acousto-magneto-plasmonics," Nat. Phot. **6** (2012).
11. V. I. Belotelov, L. L. Doskolovich, and A. K. Zvezdin, "Extraordinary magneto-optical effects and transmission through metal-dielectric plasmonic systems," Phys. Rev. Lett. **98**, 077401–1–4 (2007).
12. V. I. Belotelov, D. A. Bykov, L. L. Doskolovich, A. N. Kalish, and A. K. Zvezdin, "Extraordinary transmission and giant magneto-optical transverse Kerr effect in plasmonic nanostructured films," J. Opt. Soc. Am. B **26**, 1594–1598 (2009).
13. L. Halagačka, M. Vanwolleghem, K. Postava, B. Dagens, and J. Pištora, "Anomalous switching of giant magnetoplasmonic transverse kerr effect," J. Magn. Soc. Jpn. **26**, 78–81 (2012).
14. L. Halagačka, M. Vanwolleghem, K. Postava, B. Dagens, and J. Pištora, "Coupled mode enhanced giant magnetoplasmonics transverse Kerr effect," Opt. Express **21**, 21741–21755 (2013).
15. V. Belotelov, I. Akimov, M. Pohl, V. Kotov, S. Kasture, A. Vengurlekar, A. Gopal, D. Yakovlev, A. Zvezdin, and M. Bayer, "Enhanced magneto-optical effect in magnetoplasmonic crystal," Nat. Nanotechnol. **6**, 370–376 (2011).
16. I. A. Akimov, V. I. Belotelov, A. V. Scherbakov, and M. Pohl, "Hybrid structures of magnetic semiconductors and plasmonic crystals: a novel concept for magneto-optical devices." J. Opt. Soc. Am. B **29**, A103–A118 (2012).
17. M. Pohl, V. I. Belotelov, I. A. Akimov, S. Kasture, A. S. Vengurlekar, A. V. Gopal, A. K. Zvezdin, D. R. Yakovlev, and M. Bayer, "Plasmonic crystals for ultrafast nanophotonics: Optical switching of surface plasmon polaritons," Phys. Rev. B **85**, 081401 (2012).
18. L. Halagačka, M. Vanwolleghem, F. Vaurette, J. Ben-Youssef, P. Gogol, N. Yam, K. Postava, B. Dagens, and J. Pištora, "Experimental demonstration of anomalous nonreciprocal optical response of 1D periodic magnetoplasmonic nanostructures," Proc. SPIE **8988**, 89880E–89880E–6 (2014).
19. L. Li, "Reformulation of the Fourier modal method for surface–relief gratings made with anisotropic materials," J. Mod. Opt. **45**, 1313–1334 (1998).
20. H. Raether, "Surface plasmons on smooth and rough surfaces and on gratings", vol. 111 of "Springer Tracts in Modern Physics" (Springer-Verlag, 1988).
21. R. H. Ritchie, E. T. Arakawa, J. J. Cowan, and R. N. Hamm, "Surface-plasmon resonance effect in grating diffraction," Phys. Rev. Lett. **21**, 1530–1533 (1968).
22. E. Garcia-Caurel, R. Ossikovski, M. Foldyna, A. Pierangelo, A. De Martino, and B. Drévillon, "Advanced Mueller Ellipsometry Instrumentation and Data Analysis." in "Ellipsometry at the nanoscale," , Springer, ed. (Springer, 2013), Engineering, p. 31.
23. J. Ben Youssef, A. Thiaville, O. Navarro, J. M. Desvignes, and H. Le Gall, "Material considerations for vertical Bloch lines direct observation and dynamical study," IEEE Trans. Magn. **27**, 5505–5507 (1991).
24. V. Kravtchenko, J. Desvignes, H. L. Gall, and J. Cerceau, "Growth and magnetooptical properties of thin garnets films in the system (Pr Gd Yb)$_{3-x}$Bi$_x$(Fe Al)$_5$O$_{12}$," Mater. Res. Bull. **14**, 559 – 565 (1979).
25. J. M. Decitre, M. Lemistre, J. B. Youssef, F. Lepoutre, D. Placko, and P. Joubert, "Magneto-optical imaging method and device," (2007). US patent No. 7271900.
26. B. Ferrand, M. Armand, H. Moriceau, J. Daval, and J. Gay, "Growth of high figure of merit magnetic garnet films for magneto-optical applications," Mater. Res. Bull. **21**, 633 – 638 (1986).
27. G. E. Jellison Jr., V. I. Merkulov, A. A. Puretzky, D. B. Geohegan, G. Eres, D. H. Lowndes, and J. B. Caughman, "Characterization of thin-film amorphous semiconductors using spectroscopic ellipsometry," Thin Solid Films **377-378**, 68–73 (2000).
28. M. Foldyna, K. Postava, J. Bouchala, J. Pistora, and T. Yamaguchi, "Model dielectric functional of amorphous materials including Urbach tail," Proc. SPIE **5445**, 301–305 (2004).
29. A. S. Ferlauto, G. M. Ferreira, J. M. Pearce, C. R. Wronski, R. W. Collins, X. Deng, and G. Ganguly, "Analytical

#215021 - $15.00 USD Received 1 Jul 2014; revised 30 Jul 2014; accepted 30 Jul 2014; published 22 Aug 2014

model for the optical functions of amorphous semiconductors from the near-infrared to ultraviolet: Applications in thin film photovoltaics," J. Appl. Phys. **92**, 2424–2436 (2002).
30. D. E. Aspnes, "Local-field effects and effective-medium theory: A microscopic perspective," Am. J. Phys. **50**, 704–709 (1982).
31. P. J. Roussel, J. Vanhellemont, and H. E. Maes, "Numerical aspects of the implementation of the effective-medium approximation models in spectroscopic ellipsometry regression software," Thin Solid Films **234**, 423–427 (1993).
32. K. Postava, H. Sueki, M. Aoyama, T. Yamaguchi, C. Ino, and Y. Igasaki, "Spectroscopic ellipsometry of epitaxial ZnO layer on sapphire substrate," J. Appl. Phys. **87**, 7820–7824 (2000).
33. L. Li, "Formulation and comparison of two recursive matrix algorithms for modeling layered diffraction gratings," J. Opt. Soc. Am. A **13**, 1024–1035 (1996).
34. L. Li, "Use of Fourier series in the analysis of discontinuous periodic structures," J. Opt. Soc. Am. A **13**, 1870–1876 (1996).
35. G. E. Jellison Jr. and F. A. Modine, "Parameterization of the functions of amorphous materials in the interband region," Appl. Phys. Lett. **69**, 371–373,2137 (1996).
36. L. E. Kreilkamp, V. I. Belotelov, J. Y. Chin, S. Neutzner, D. Dregely, T. Wehlus, I. A. Akimov, M. Bayer, B. Stritzker, and H. Giessen, "Waveguide-plasmon polaritons enhance transverse magneto-optical kerr effect," Phys. Rev. X **3**, 041019 (2013).
37. T. Goto, M. C. Onbaşli, and C. A. Ross, "Magneto-optical properties of cerium substituted yttrium iron garnet films with reduced thermal budget for monolithic photonic integrated circuits," Opt. Express **20**, 28507–28517 (2012).
38. P. Hansen, K. Witter, and W. Tolksdorf, "Magnetic and magneto-optic properties of lead- and bismuth-substituted yttrium iron garnet films," Phys. Rev. B **27**, 6608–6625 (1983).
39. S. Wittekoek, T. J. A. Popma, J. Robertson, and P. Bongers, "Magneto-optic spectra and the dielectric tensor elements of bismuth-substituted iron garnets at photon energies between 2.2-5.2 eV," Phys. Rev. B **12**, 2777–2788 (1975).
40. T. Boudiar, B. Payet-Gervy, M.-F. Blanc-Mignon, J.-J. Rousseau, M. L. Berre, and H. Joisten, "Magneto-optical properties of yttrium iron garnet (YIG) thin films elaborated by radio frequency sputtering," J. Magn. Magn. Mater. **284**, 77 – 85 (2004).
41. A. H. Eschenfelder, "Magnetic bubble technology" (Berlin ; New York : Springer-Verlag, 1980).
42. Š. Višňovský, "Optics in magnetic multilayers and nanostructures," (CRC,2006).
43. G. Scott and D. E. Lacklison, "Magnetooptic properties and applications of bismuth substituted iron garnets," IEEE Trans. on Mag. **12**, 292–311 (1976).
44. G. B. Scott, D. E. Lacklison, H. I. Ralph, and J. L. Page, "Magnetic circular dichroism and faraday rotation spectra of $Bi_3Fe_5O_{12}$," Phys. Rev. B **12**, 2562–2571 (1975).
45. M. Foldyna and A. D. Martino, "Characterization of grating structures by Mueller polarimetry in presence of strong depolarization due to finite spot size," Opt. Commun. **282**, 735–741 (2009).
46. P. B. Johnson and R. W. Christy, "Optical constants of the noble metals," Phys. Rev. B **6**, 4370–4379 (1972).
47. M. Khashan and A. Nassif, "Dispersion of the optical constants of quartz and polymethyl methacrylate glasses in a wide spectral range: $0.2 - 3$ μm," Opt. Commun. **188**, 129 – 139 (2001).

1. Introduction

The magneto-optical (MO) garnets were studied for decades for systems with the non-reciprocal optical response, i.e. for systems with the broken time-reversal symmetry. In the near infra-red region the garnets are commonly used for their sufficiently large MO effect, low optical absorptions [1] and compatibility with III-V semiconductor and silicon technology. For the optical telecommunication wavelength of 1550 nm several concepts of integrated structures with non-reciprocal optical response, i.e. optical isolators and circulators, were proposed [2, 3]. Impressive work in optical isolation based on MO garnets in combination with silicon waveguiding systems with ring resonators or Mach-Zehnder interferometer was presented by Mizumoto et.al [4–6] and Fujita et. al. [7, 8]. The monolithic nonreciprocal optical-resonator-based isolator with high isolation ration combining MO garnet on a single-mode silicon waveguide was recently demonstrated by Bi and Ross [9].

In a free-space configuration the MO garnet response can be further enhanced by a plasmonic gold grating, i.e. grating supporting effect of surface plasmon polariton (SPP) excitation [10]. In particular, it has been predicted and demonstrated that the nonreciprocal splitting of the extraordinary reflection (and transmission) spectra of a 1D plasmonic gold grating on a transversely

#215021 - $15.00 USD Received 1 Jul 2014; revised 30 Jul 2014; accepted 30 Jul 2014; published 22 Aug 2014

magnetized MO substrate, leads to a giant enhancement of the transverse magneto-optic Kerr (TMOKE) response of such a magnetoplasmonic structure [11–13]. It was explained how the nonreciprocal splitting of the dispersion of the SPP's guided by the garnet/Au grating interface causes a nonreciprocal shift of the Wood-plasmon resonances, the extraordinary optical transmission (EOT), reflection spectrum of this structure, and hence is at the origin of the Kerr effect enhancement. Moreover, it was theoretically demonstrated, that TMOKE response of the magnetoplasmonic structure can be further enhanced by the proper tuning of the interaction between resonant modes in the grating, the SPPs, and the cavity resonance in the air-gaps of the grating. The optimal degree of modes interaction can be achieved by the optimization of the structure geometry [14]. Therefore there is need to characterize geometry of fabricated structure in order to optimize the design with respect to fabrication technology. The knowledge of the optical function of used materials is crucial for characterization of the fabricated structure geometry and its further optimization.

In this paper we present precise magneto-optical and optical characterization of such a 1D periodic magnetoplasmonic structure based on a gold grating prepared on a MO Bi-substituted iron garnet film $Gd_{1.24}Pr_{0.48}Bi_{1.01}Lu_{0.27}Fe_{4.38}Al_{0.6}O_{12}$ (Bi:GIG) and a (CaMgZr)-doped gallium-gadolinium garnet (sGGG) substrate. Knowledge of the optical and magneto-optical functions of the materials is essential for structure modeling and further analysis of the experimental data. Despite the fact that the optical and the MO response of such a structure has been under deep theoretical [12–14] and experimental study [15–18] a direct comparison between a fitted model of the real structure and experimental data has not been presented yet. It is the goal of this paper to present a model of the structure that takes into account fabrication imperfections and that fits well to experimental optical and magneto-optical Mueller matrix data. The optical response of the grating has been calculated using own developed software that implements a fully vectorial anisotropic rigorous coupled wave algorithm (RCWA) [19]. In the end, such a successful fitting would not only validate the theoretical assumption about the origin of the plasmonic enhancement of the TMOKE but would also demonstrate the validity and the potential of the numerical tool. Moreover, the spectral characterization of the gyrotropy and the permittivity of Bi:GIG is useful for the design of future nonreciprocal components.

The paper is organized as follows. In Section 2 a principle of surface plasmon generation in magnetoplasmonic grating is summarized. The experimental technique (Mueller matrix ellipsometry), the sample composition, and the fabrication process of the grating are introduced in Sec. 3. In Section 4 we present characterization of the optical functions of the sGGG and Bi:GIG from transmission spectra and reflection Mueller matrix spectra. In Section 5 the magneto-optical properties of the Bi:GIG layer are determined from the Mueller matrix spectra measured in both transverse and longitudinal MO configurations. Finally, Section 6 deals with the optical characterization of the gold grating geometry allowing for fabrication imperfections in the model fit. The obtained values for the grating parameters (and its fabrication imperfections) were subsequently used together with the measured MO and optical functions of the garnet layers to compare the measured and calculated MO response (Sec. 6.2).

2. Principle of magnetoplasmonics gratings

The transverse magneto-optic response of the plasmonic grating originates from enhancement of TMOKE effect in MO Bi:GIG by SPP modes excited at the Au/Bi:GIG interface. The dispersion of the wavevector tangential component of the SPP resonances at a simple interface between gold and Bi:GIG are described by the relation [20]:

$$k_{\mathrm{SP}}(E) = \frac{2\pi}{hc} E \sqrt{\frac{\varepsilon_{\mathrm{Au}}(E)\,\varepsilon_{\mathrm{Bi:GIG}}(E)}{\varepsilon_{\mathrm{Au}}(E) + \varepsilon_{\mathrm{Bi:GIG}}(E)}}, \tag{1}$$

#215021 - $15.00 USD Received 1 Jul 2014; revised 30 Jul 2014; accepted 30 Jul 2014; published 22 Aug 2014

where E is the photon energy and $\varepsilon_{\mathrm{Au}}(E)$, $\varepsilon_{\mathrm{Bi:GIG}}(E)$ represent the permittivity of gold and Bi:GIG, respectively. To achieve appropriate tangential component of the wavevector one can usually use Kretschmann configuration with high-refractive index prism or a higher-order diffraction mode in grating. In the 1D periodic structure the SPP is excited by the diffracted wave:

$$k_W(E) = \pm k_{\mathrm{SP}}(E) + m\frac{2\pi}{\Lambda}, \text{ with } m \in \mathbb{Z}, \tag{2}$$

where k_W denotes the wavevector of the SPP and m is the order of diffracted wave. This SPP excitation is historically known as a *Wood plasmon*, because it was observed close to Wood-Rayleigh anomalies [21]. Note that surface plasmon resonances occurs only for *p*-polarization. Spectral positions of the SPP peaks in magnetoplasmonic structure are shifted by the TMOKE in the Bi:GIG [11–14]. Since the SPP resonance leads to field confinement at MO Bi:GIG/Au interface the TMOKE effect is significantly enhanced.

3. Experimental technique and sample composition

3.1. Experimental setup and measured quantities

The spectroscopic Mueller matrix ellipsometer Woollam RC2-DI (J.A. Woollam Co.) consisting of dual rotating compensators was employed in a wide spectral range from 0.74 eV to 6.42 eV (wavelength region from 193 nm to 1.7 μm). The PCSCA (Polarizer-Compensator-Sample-Compensator-Analyzer) configuration was used. Figure 1 shows the ellipsometric configuration, the orientation of coordinate system, and in-plane magnetization components schematically.

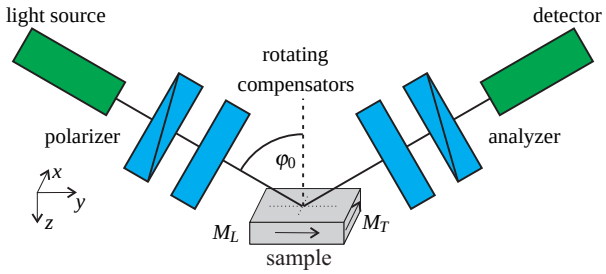

Fig. 1. Dual-rotating compensator ellipsometer configuration and orientation of external in-plane magnetization components are shown schematically.

The interaction of the light beam with a general (anisotropic, depolarizing) sample is described with a full 4×4 Mueller matrix [22]. In the case of an isotropic structure, the normalized reflection Mueller matrix is given in the block-diagonal form:

$$\mathbf{M} = \begin{bmatrix} 1 & -N & 0 & 0 \\ -N & 1 & 0 & 0 \\ 0 & 0 & C & -S \\ 0 & 0 & S & C \end{bmatrix}. \tag{3}$$

The Mueller matrix (3) is normalized with respect to the element M_{11}, which describes total reflection intensity for completely unpolarized light. In case of system without depolarization the elements N,C, and S are related to the classical ellipsometric angles ψ and Δ:

$$N = \cos 2\psi, \quad C = \sin 2\psi \sin\Delta, \quad S = \sin 2\psi \cos\Delta, \tag{4}$$

#215021 - $15.00 USD Received 1 Jul 2014; revised 30 Jul 2014; accepted 30 Jul 2014; published 22 Aug 2014

where ellipsometric angles ψ and Δ are defined by the ration of complex reflection coefficients:

$$r_{pp}/r_{ss} = \tan\psi \exp(\mathrm{i}\Delta). \quad (5)$$

For a precise determination of the dielectric function of the sGGG substrate we have combined the spectroscopic data from reflection ellipsometry and transmission spectroscopy. Including also the transmission data gives us additional information about absorption and position of a possible band-gap. For characterization of the optical function of the Bi:GIG layer we have used micro focusing probes with a focal length of 27 mm to reduce the spot size to approximately 150 μm. Using a focused beam allows to reduce the influence of the thickness inhomogeneity of the sample in the area of the beam spot. Moreover the effect of back-side refection in the thick sGGG substrate was eliminated as well.

3.2. Substrate description and fabrication

Single crystal films of Bi-substituted iron garnets were grown by Liquid Phase Epitaxial (LPE) procedures onto doped sGGG (111) oriented substrates. The exact composition of the sGGG substrate is $Gd_{2.7}Ca_{0.3}Ga_{4.1}Mg_{0.3}Zr_{0.6}O_{12}$. For magneto-optical devices, both the optical figure of merit and the magnetic properties such as magnetization and anisotropy must be controlled. We prepare rare earth (RE) substituted films by combination of Gd, Pr, Lu on CaMgZr-GGG substrates with large lattice parameter ($a_S = 12.498$ Å) in order to incorporate a large content of Bi and thus induce a large Faraday rotation. Low in-plane anisotropy is necessary to obtain an easy switching of the magnetization. By the electron micro probe analysis (EPMA) the chemical composition of the Bi:GIG was determined as: $Gd_{1.24}Pr_{0.48}Bi_{1.01}Lu_{0.27}Fe_{4.38}Al_{0.6}O_{12}$. The role of each ion is the following: substituted-gadolinium garnet has been selected since large Bi content can be introduced in such a host [23–25]. Praseodymium ions have high contribution to the Faraday rotation but their main contribution remains the reduction of the anisotropy constant [26]. A similar result can be obtained with Nd^{3+} ions. The saturation magnetization is reduced to the selected value by the substitution of Fe^{3+} by non-magnetic ions. The best choice is obtained with Al^{3+} ions with a smaller content compared to Ga3+ in order to match the lattice parameters of the film and substrate. A perfect surface with a low roughness is obtained with this substituted garnet grown at a low ΔT , where $\Delta T = T_s - T_g$ is the supercooling temperature, T_s is the saturation temperature and T_g a growth temperature. For good surface quality films, a low T_g and generally low growth rates are common features of all melts for incorporation of larger Bi content.

3.3. Magnetoplasmonic grating fabrication

The gold grating structure was fabricated by Au evaporation on a mask written by e-beam lithography in the positive poly-methyl metacrylate (PMMA) resist. The spin-coated PMMA resist has been baked for 10 min at 180° C. Instead of conducting resist a 5 nm thick layer of germanium was used. $300 \times 300\mu$m rectangular patch of 1D grating was written by electron beam lithography with the exposure dose 1040 μC/cm^2. The period of the grating was kept fixed at $\Lambda = 500$ nm. After e-beam writing, the germanium layer was removed by a 1:1 solution of H_2O_2/H_2O for 1 min. In the next step the sample was developed in MIBK/IPA (methyl isobutyl ketone/isopropyl alcohol) in ratio 1:2, for 1 minute. Finally, the Au layer with a thickness of approximately 100nm has been evaporated on the developed resist and the grating structure was obtained by lift-off in an ultrasonic bath of SVC14 remover for 1 hour.

4. Optical functions of sGGG substrate and Bi:GIG layer

The first step in obtaining a successful fitting of the magneto-optic response of a nanostructured (magneto-)optical system to a structural model, is a precise determination of the material dis-

#215021 - $15.00 USD Received 1 Jul 2014; revised 30 Jul 2014; accepted 30 Jul 2014; published 22 Aug 2014

persion of the composing materials. The optical functions (i.e. the diagonal permittivity tensor components) of the sGGG substrate and the Bi:GIG layer are determined using a combination of Mueller matrix ellipsometry and transmission spectroscopy. The critical step involved in fitting spectroscopic ellipsometric data to a given structural model is the proper parametrization of the dispersion of the unknown optical functions. We have used a Kramers-Krönig (KK) consistent Tauc-Lorentz (TL) model and its extension with an Urbach tail (TLU). The imaginary part of the complex dielectric function $\varepsilon = \varepsilon_1 - \mathrm{i}\varepsilon_2$ is defined:

$$\varepsilon_2(E) = \begin{cases} \dfrac{1}{E}\dfrac{AE_0C(E-E_g)^2}{(E^2-E_0^2)^2+C^2E^2} & E \geq E_c \\ \\ \dfrac{A_u}{E}\exp\left(\dfrac{E}{E_u}\right) & 0 \leq E \leq E_c \end{cases}, \tag{6}$$

where the first term $(E \geq E_c)$ is identical with Tauc-Lorentz function [27] and the second term $(0 \leq E \leq E_c)$ represents the exponential Urbach tail. Parameters E_g, A, E_0, and C denote the band gap energy, the amplitude, the Lorentz resonant frequency, and the broadening parameter, respectively. Parameters A_u and E_u are chosen with respect to continuity of first derivatives. The real part ε_1 of the dielectric function is obtained using analytical integration of KK relations. For more details of derivation of the TLU model see [28]. To fit the spectroscopic data of sGGG and Bi:GIG the combination of the TL and TLU model were used to describe shape of absorptions near the band gap. The advantage of the TLU model is, that it is parametrized by five parameters instead of seven as the (common) Cody-Lorentz model [29].

In our article, the the Bruggeman effective medium approximation (BEMA) of the mixture of hosting material (ε) with void was used to simulate surface roughness as a thin layer with effective permittivity $\varepsilon_{\mathrm{eff}}$ defined [30, 31]:

$$0 = (1-f)\,\frac{\varepsilon - \varepsilon_{\mathrm{eff}}}{\varepsilon + 2\varepsilon_{\mathrm{eff}}} + f\,\frac{1-\varepsilon_{\mathrm{eff}}}{1+2\varepsilon_{\mathrm{eff}}}, \tag{7}$$

where f is the volume fraction.

The measured data were fitted using a Levenberg-Marquardt least square algorithm. The Poincaré sphere representation of the difference between experimental and model data were used in the analysis [32]. The optical response has been calculated using own developed software that implements a fully vectorial anisotropic rigorous coupled wave method (RCWA) [19]. For 1D periodic structures the code uses S-matrix formalism [33] and better convergence is achieved by factorization of Fourier series expansion [34].

4.1. Ellipsometric and transmission spectra on sGGG substrate

Figure 2 shows experimental data obtained on a 0.5 mm thick sGGG planar substrate. For these measurements a collimated beam instead of a focused beam has been used. This is more suitable for the detection of fine spectral features in the absorption of the bulk substrate. Both sides of the substrate have been polished, therefore incoherent reflections from the back-side of the substrate have been included in the model. Ellipsometric data [obtained using Eq. (3)] were measured at an incidence angle of $\varphi_0 = 45^\circ$, while the transmission was measured at normal incidence. Surface roughness from both sides of the substrate was represented by a thin film with thickness to be fitted and a permittivity given by the BEMA [Eq. (7)] with a fixed volume fraction $f = 0.5$ (mixture of both media in ratio 50 %–50 %). The optical functions of the sGGG were parametrized using two Tauc-Lorentz absorptions [35] with the same band-gap energy E_g extended by Urbach absorption tail [Eq. (6)] and one damped harmonic oscillator (DHO) as

#215021 - $15.00 USD Received 1 Jul 2014; revised 30 Jul 2014; accepted 30 Jul 2014; published 22 Aug 2014

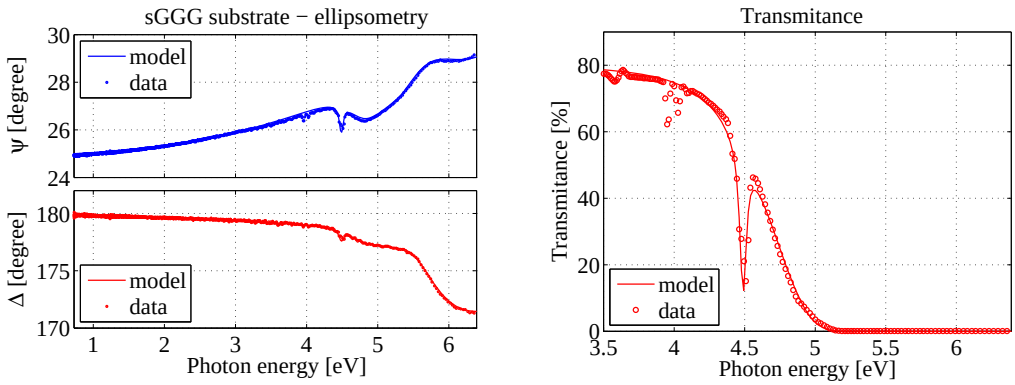

Fig. 2. Measured spectra (dots) of ellipsometric angles ψ (top left), Δ (bottom left) and transmittance (right subplot) are compared with the model (lines).

follows:

$$\varepsilon_{\mathrm{sGGG}} = \varepsilon_{TL} + \varepsilon_{TLU} + \varepsilon_{DHO}, \tag{8}$$

where ε_{TL} and ε_{TLU} are contributions from TL and TLU functions with common band gap energy and ε_{DHO} is the damped harmonic oscillator defined :

$$\varepsilon_{DHO}(E) = \frac{AE_0^2}{E_0^2 - E^2 + \mathrm{i}CE}, \tag{9}$$

where A is the amplitude, E_0 is the central energy, and C is the damping parameter.

The best fit parameters are summarized in Table 1 and the modeled ellipsometric and transmission spectra are presented by solid lines in Fig. 2. Figure 3 shows resulting dielectric functions of the sGGG substrate. Note that the even small contribution of the DHO at 4.49eV is visible in ellipsometric and transmission spectra due to long propagation length in transparent material. Precise knowledge of the substrate optical functions is crucial for precise characterization of the MO Bi:GIG layer and the further data fit from the magnetoplasmonic grating structure.

Table 1. Parameters of model of sGGG substrate

	ε_∞	E_g [eV]	A	E_0 [eV]	C [eV]	E_c [eV]
TLU:	1.90	5.35	105.48	7.93	0.54	5.89
TL:	0	5.35	173.39	5.67	1.08	
DHO:			$2.52 \cdot 10^{-6}$	4.49	0.0392	
surf. roughness - BEMA:	$t = 2.89$ nm		$f = 0.5$			

4.2. Ellipsometric spectra on Bi:GIG layer

Figure 4 shows the ellipsometric spectra ($\varphi_0 = 45°$) measured on an approximately 4μm thick Bi:GIG layer, grown by LPE on a sGGG substrate as explained in Sec. 3.2. The observed strong interference oscillations indicate the presence of an absorption gap close to 2.5 eV. Because of these it is difficult to obtain a good fit to an analytical material model over the whole measured spectrum. The optical functions of Bi:GIG were therefore determined in a two-step procedure. In the first step, only the data in the range below 2.5 eV were fitted to a model describing the

#215021 - $15.00 USD Received 1 Jul 2014; revised 30 Jul 2014; accepted 30 Jul 2014; published 22 Aug 2014

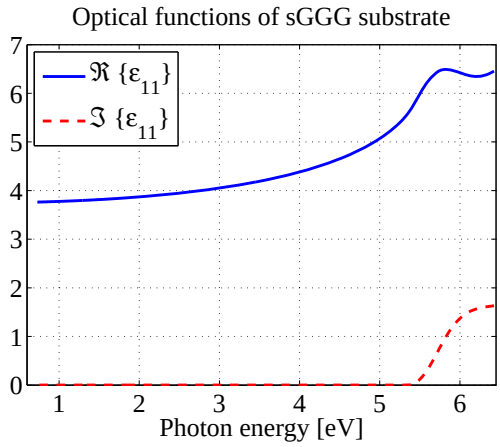

Fig. 3. Optical functions of sGGG substrate. The real part $\Re\{\varepsilon_{11}\}$ and the imaginary part $\Im\{\varepsilon_{11}\}$ of the function is plotted using solid and dashed lines, respectively.

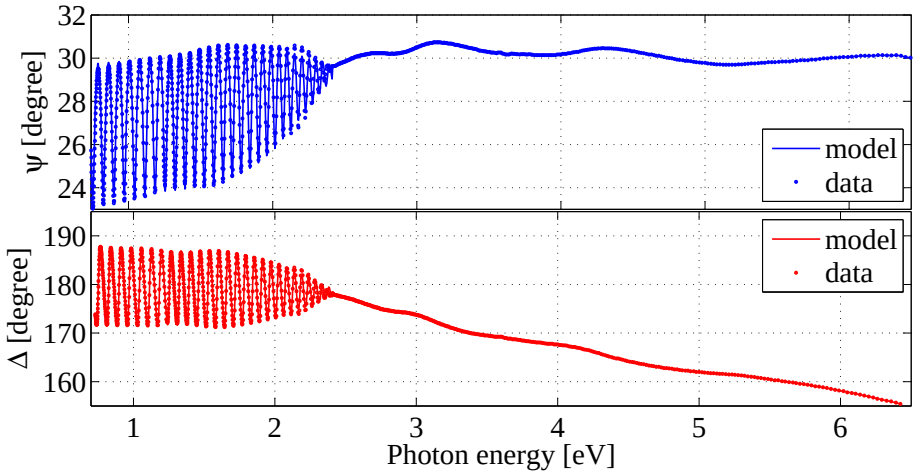

Fig. 4. Measured ellipsometric angles of Bi:GIG layer on sGGG substrate (dots) are compared with model (lines).Upper and lower subplot corresponds to ψ and Δ respectively.

dispersion of Bi:GIG using Tauc-Lorentz-Urbach parametrization. Again surface roughness at the top of the epitaxial Bi:GIG layer and a possible intermixing layer at the Bi:GIG/sGGG interface were included and described using BEMA with a volume fraction $f = 0.5$ (mixture of both media in ratio 50%–50%) (7). Using a focused beam, the sGGG substrate could be considered as a semi-infinite substrate with a permittivity as determined in Sec. 4.1. The thickness of the Bi:GIG layer was fitted. The focusing probes introduce a certain angular spread on the incidence angle. In the transparent region this can have a profound impact on the spectral position and the finesse of the interference fringes. This spread φ_s was therefore also considered as a fitting parameter. Table 2 shows the best fit parameters for this TLU model of the Bi:GIG film (below 2.5eV). In the second step, the permittivity of Bi:GIG in the absorbing spectral range was calculated by a point-by-point fitting procedure using the surface roughness and the thickness obtained in the first step. Figure 5 shows total dielectric functions of Bi:GIG layer in the whole spectral range.

#215021 - $15.00 USD Received 1 Jul 2014; revised 30 Jul 2014; accepted 30 Jul 2014; published 22 Aug 2014

Table 2. Parameters of model of Bi:GIG layer on sGGG substrate, 0.74 - 2.5 eV.

	ε_∞	E_g [eV]	A	E_0 [eV]	C	E_c [eV]
TLU:	3.39	0.21	8.62	3.64	0.48	3.39
surf. roughness - BEMA:		$t = 2.89$ nm	$f = 0.5$			
Bi:GIG thickness:		$t = 3988.4$ nm				
sGGG/Bi:GIG intermix - BEMA:		$t = 3.94$ nm	$f = 0.5$			
angular spread:		$\varphi_s = 1.70^\circ$				

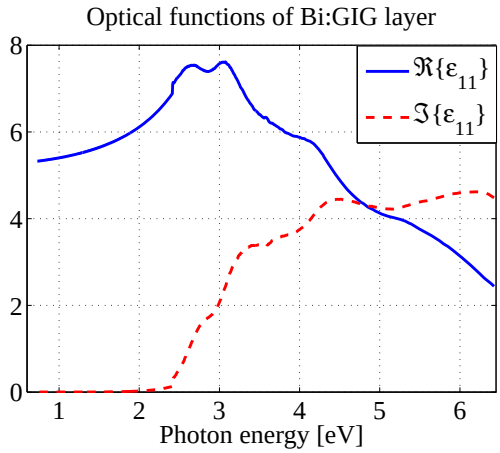

Fig. 5. Optical function of Bi:GIG layer. The real part $\Re\{\varepsilon_{11}\}$ and the imaginary part $\Im\{\varepsilon_{11}\}$ of the function is plotted using solid and dashed lines, respectively.

5. Magnetooptical properties of Bi:GIG in transverse and longitudinal MO configuration

Knowledge of the Bi:GIG gyrotropy, $g = \varepsilon_{yz}$ (if the garnet is magnetized along the $+x-$direction) is crucial for the design and characterization of the magnetoplasmonic grating described 6.2. To be able to characterize the MO properties of the Bi:GIG film, the Mueller matrix ellipsometer was extended with an in-plane magnet circuit consisting of a permanent magnet mounted on a rotary stage. This was driven by a computer-controlled servomotor, which made the experiment repeatable with high accuracy. The permanent magnet delivered a sufficiently uniform 300 Oe in a volume enclosing the sample holder, 20 mm spacing between magnet poles. This is largely sufficient for in-plane magnetic saturation of the Bi:GIG [36–39], as testified by the $M-H$ hysteresis loop of Faraday effect measured in transmission through the sample with in-plane external magnetic field and the angle of incidence of 45° shown in Fig. 6. This underlines also the planar magnetic anisotropy and the softness of the elaborated garnet material ($H_c = 0.5$ Oe). Figure shows, that magnetic field of 300 Oe used in our MO analysis is height-enough for in-plane magnetic saturation.

Because the thickness of the Bi:GIG layer is not perfectly uniform and because the MO characterization was performed with focusing probes in different area of the sample, the thickness of the Bi:GIG layer was re-fited from optical measurement performed as the first step. The new obtained thickness of Bi:GIG layer measured with focusing optics was 3973.6 nm. This is close to the previously fitted thickness 3988.4 nm measured with collimated beam. This step was necessary to perform, otherwise even a small difference between interference peaks in calculation

#215021 - $15.00 USD Received 1 Jul 2014; revised 30 Jul 2014; accepted 30 Jul 2014; published 22 Aug 2014

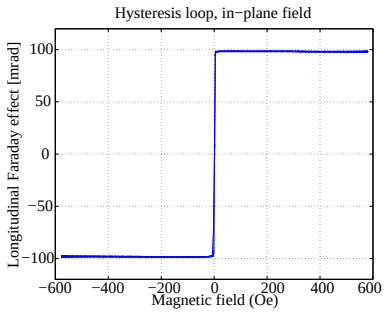

Fig. 6. Hysteresis loop of Faraday effect measured in transmission through the sample for in-plane external magnetic field and the angle of incidence of 45°.

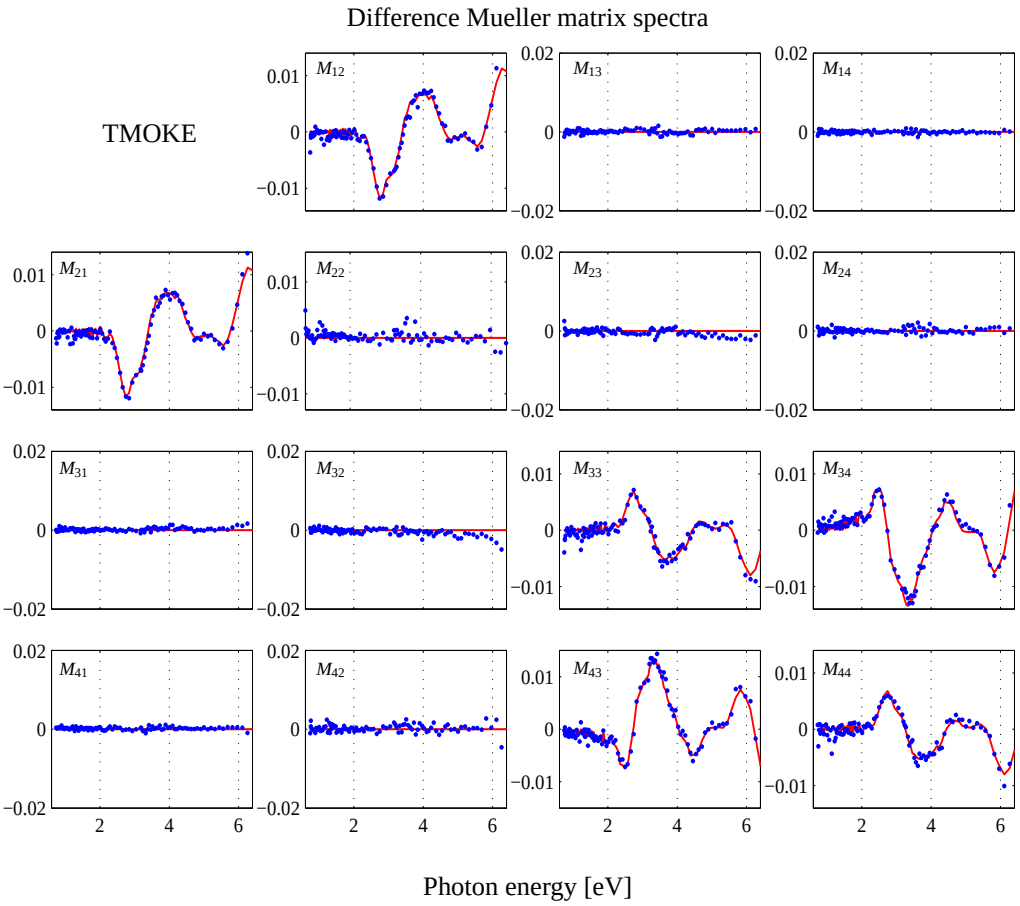

Fig. 7. Measured differences of the Mueller matrix components obtained from MO measurements in transverse MO configuration (blue dots) are compared with the model (red lines). Reduced number of spectral points is shown in order to distinct the measured data from model.

#215021 - $15.00 USD Received 1 Jul 2014; revised 30 Jul 2014; accepted 30 Jul 2014; published 22 Aug 2014

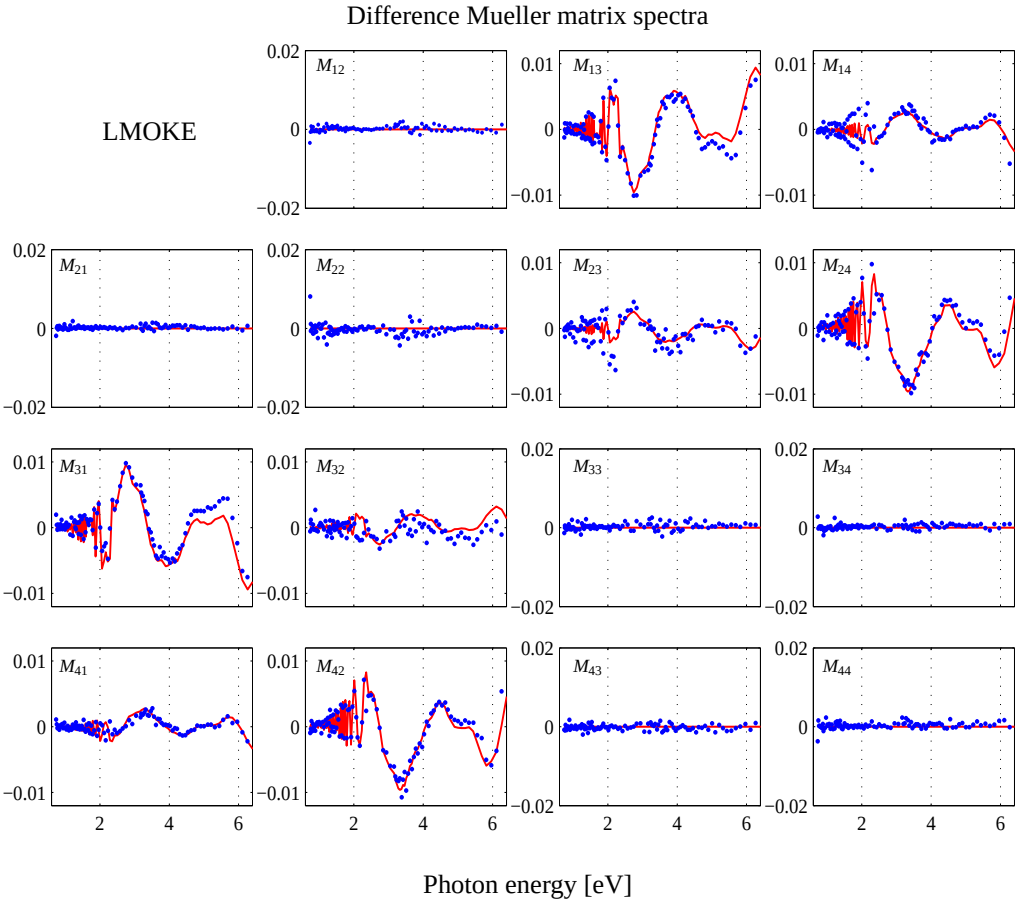

Fig. 8. Measured differences of the Mueller matrix components obtained from MO measurements in longitudinal MO configuration (blue dots) are compared with the model (red lines). Reduced number of spectral points is shown in order to distinct the measured data from model.

and measurement would introduce oscillations into fitted off-diagonal optical functions. In the model we have used the optical functions of Bi:GIG and sGGG determined in Sec. 4 . In the second step the in-plane magnet was installed and the magnetization was applied both in the transverse ($M_T^{\text{sat.}}$) and the longitudinal ($M_L^{\text{sat.}}$) MO configuration (see coordinate system on Fig. 1). After each spectrum measurement the orientation of the magnetization was reversed. Each specific MO configuration (transverse or longitudinal, either “up” or “down”) was averaged over five measurements in order to reduce random noise and increase measurement sensitivity. Subtraction of the averaged data for opposite magnetization then leads to the differential Mueller matrices:

$$\mathbf{M}_x^{\text{diff.}} = \mathbf{M}\left(+M_x^{\text{sat.}}\right) - \mathbf{M}\left(-M_x^{\text{sat.}}\right), \quad x = T, L. \tag{10}$$

In the next step, the gyrotropy of Bi:GIG was calculated by a point-by-point fitting procedure from the transverse and longitudinal spectra of the difference Mueller matrices. Because the crystalline structure of Bi:GIG is cubic, the MO parameters fitted from TMOKE ($\mathbf{M}_T^{\text{diff.}}$) and LMOKE ($\mathbf{M}_L^{\text{diff.}}$) difference Mueller matrix spectra are equivalent [40,41]. In order to increase

#215021 - $15.00 USD Received 1 Jul 2014; revised 30 Jul 2014; accepted 30 Jul 2014; published 22 Aug 2014

the quality of the fit the TMOKE and LMOKE data were used in the fitting procedure together.

Figure 7 shows comparison of the measured and calculated TMOKE difference data. The TMOKE affects only *p*-reflectivity and does not lead to a polarization conversion.Therefore the differential Mueller matrices must be block-diagonal $\mathbf{M}_T^{\text{diff.}}$, since these elements contain only the signature of the diagonal Fresnel coefficients, r_{ss}, and r_{pp} (Fig. 7). On the other hand, the LMOKE response is detected only in off-diagonal blocks, namely the components $M_{13}, M_{14}, M_{23}, M_{24}, M_{31}, M_{32}, M_{41}$, and M_{42}. This corresponds to conversion between *s*- and *p*-polarized light. The block-diagonal elements are zero up to first order due to the substraction of the isotropic part of the LMOKE reflection.

Figure 9 shows the obtained off-diagonal permittivity tensor component. The microscopic origin of the off-diagonal permittivity functions is well discussed in the paper of Wittekoek et. al. [39]. In our data shown on Fig. 9, the main MO activity is connected with peaks at 2.7 eV and 3.2 eV. The peak at 2.7 eV corresponds to the second type of transition (so called paramagnetic). The paramagnetic peak is over-beaten by the first type of transition (diamagnetic) at 3.2 eV {Chap. 2. in [42]}. The obtained spectral function of MO activity by the Mueller matrix ellipsometry is in very good agreement with results obtained for fully bismuth substituted ($x = 1$) BIG presented by Wittekoek [39] and with data presented in other papers [38, 43, 44]. It should also be noted that the observed spectral behavior of the gyrotropy is in agreement with the dielectric loss spectrum observed on the imaginary part of Fig. 5. Indeed, hermiticity of the $\varepsilon-$tensor requires the real part of the off-diagonal permittivity elements to be zero as long as the material is transparent. In accordance with the band gap observed in Fig. 9 at around 2.5eV, the real part of off-diagonal permittivity is seen to be negligible below this photon energy.

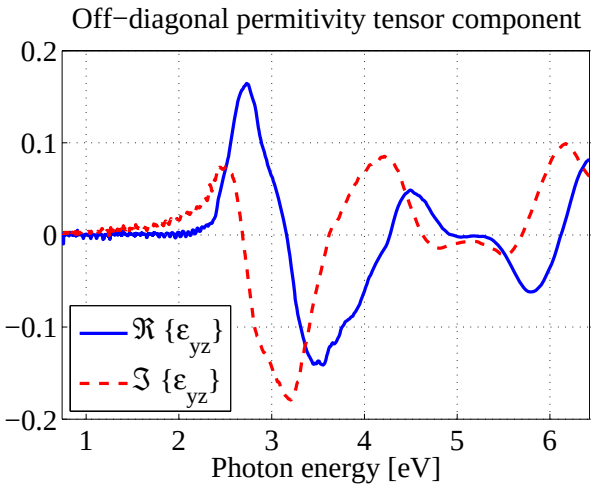

Fig. 9. Fitted spectral dependence of off-diagonal tensor component from ellipsometric measurement of Bi:GIG in transverse and longitudinal MO configuration.

6. Experimental results on magnetoplasmonic grating

With the above precise determination of the dispersion of the full permittivity tensor of both the garnet substrate and the thin film MO Bi-substituted garnet, the TMOKE response of the magnetoplasmonic grating can be analyzed. As explained its enhancement is expected to be linked to the spectral position of the different types of resonances (Fabry-Perot and Surface Plasmon) in the gold-on-garnet grating structure. Since these are highly dependent on the geometrical

#215021 - $15.00 USD Received 1 Jul 2014; revised 30 Jul 2014; accepted 30 Jul 2014; published 22 Aug 2014

parameters of the grating, it is important to verify in a first instance whether the observed resonances fit to the expected grating geometry.

6.1. *Optical characterization of the fabricated sample*

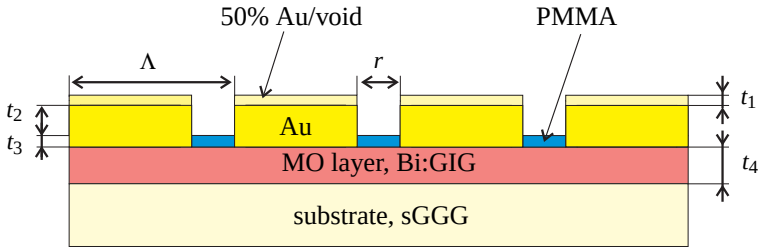

Fig. 10. Cross-section of the grating structure is shown schematically. By the fitting procedure geometrical parameters t_1-t_4, Λ, and r were estimated. Surface roughness gold/void and mixture of gold/PMMA were calculated as the BEMA layer with volume fraction $f = 0.5$.

For that purpose Fig. 10 shows the schematic representation of the grating structure indicating the chosen geometrical fitting parameters, thereby also allowing for fabrication imperfections. The following parameters are considered for fitting: the thickness of layer representing surface roughness t_1, the thickness of the gold grating $\frac{1}{2}t_1 + t_2 + t_3$, the thickness of the remaining polymethyl methacrylate (PMMA) resist inside the grating t_3, the thickness of the MO Bi:GIG layer t_4, the period Λ, and the opening of the grating r. Thickness of the layer representing surface roughness was simulated as BEMA with the fixed volume-fraction $f = 0.5$. Assumption of one half of the thickness of the surface roughness layer comes from the fixed volume fraction. Moreover, the angle of incidence φ_0 and the angular spread of the focused beam φ_s were fitted as well. Fitting of the angular spread of the focused beam was essential in the numerical analysis [45]. The divergence of the beam was modeled as a weighted sum over the incidence angle spread with expected Gaussian profile of the intensity distribution. In other worlds, the measured signal is incoherent sum of spectra obtained for all incident angles around beam divergence. This allows us to simulate reduced amplitudes of interferences of partially transmitted light in the spectral regions from approximately 630 nm to 780 nm and from 1.2 μm to 1.5 μm. The similar effect of incident angle spread appears for the main peak at $\lambda = 885$ nm. In addition a good agreement between the measured and modeled Mueller matrix components gives also proper description of the depolarization phenomena (upper-left subplot in Fig. 11).

Optical constants of the gold used in the model were estimated from ellipsometric measurements of a reference gold sample and are in good agreement with data from Johnson and Christy [46]. The dispersion of PMMA resist was taken from [47]. For the fitting of the geometrical parameters it suffices to perform only optical characterization (thus without applied magnetic field). Only after having precisely determined the fitting parameters, the TMOKE spectra will be measured. Figure 11 shows the best-fit of the Mueller matrix data measured on the fabricated grating. The optical data were measured in configuration where the plane of incidence is perpendicular to the lamelas of the grating. Therefore no *s*-*p* polarization conversion should occur and a block-diagonal arrangement of the Mueller matrix components is expected and effectively obtained. We can conclude that a possible misalignment between the grating and plane of incidence was below the sensitivity threshold of the experimental system. The first subplot compares the calculated and measured depolarization. Table 3 summarizes parameters of the model, fitted parameters are emphasized as bold symbols.

#215021 - $15.00 USD Received 1 Jul 2014; revised 30 Jul 2014; accepted 30 Jul 2014; published 22 Aug 2014

Table 3. Fitted parameters of the model shown on Fig. 10.

φ_0	=	**44.33**°	φ_s	=	**2.91**°
Λ	=	**502.6** nm	r	=	**78.68** nm
t_1	=	**13.55** nm	t_2	=	**68.16** nm
t_3	=	**23.8** nm	t_4	=	3988.4 nm

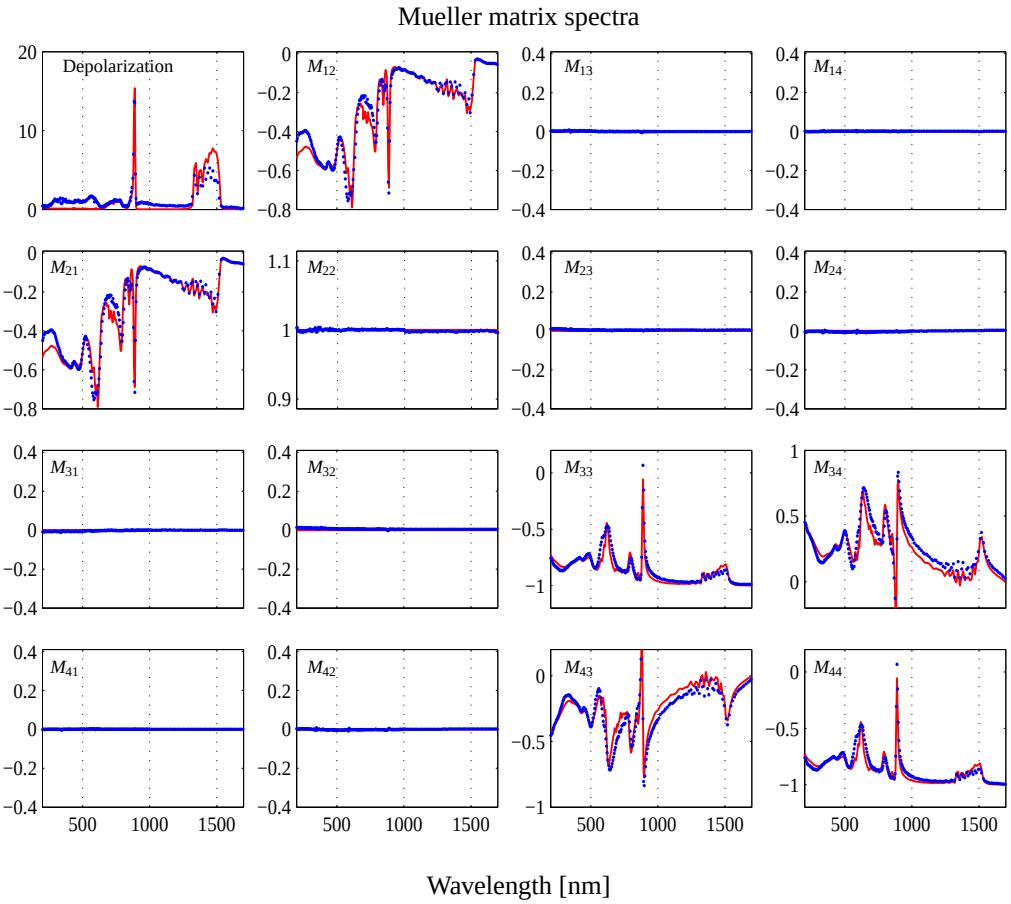

Fig. 11. Best fit of the Mueller matrix spectra measured on the plasmonic grating. Experimental data a(blue dots) are compared with numerical model (red lines). First subplot (top-left) shows good agreement between measured and calculated depolarization. A reduced number of spectral points is shown in order to distinct the measured data from model.

When using a focused beam, the angle of incidence is not exactly defined, therefore it was fitted as well. The obtained value $\varphi_0 = 44.14°$ is close to the angle of 45° set on the instrument (the difference is due to slight misalignment of the focusing optics). The nominal parameters of the sample was: the grating period $\Lambda = 500$ nm, the grating thickness $t_1 = 100$ nm, the width of air-gap $r = 63$ nm, and the thickness of the Bi:GIG $t_4 = 3988.4$ nm (from Tab. 2). The nominal width of the air-gap r was estimated from scanning electron microscopy (SEM) observation. Parameters obtained from the fit are in good agreement with nominal parameters

#215021 - $15.00 USD Received 1 Jul 2014; revised 30 Jul 2014; accepted 30 Jul 2014; published 22 Aug 2014

from fabrication process of the sample. Note, that in our parametrization of the model the total thickness of the grating is given as $\frac{1}{2}t_1 + t_2 + t_3$ =98.74 nm, the thickness of the surface roughness t_1 was taken as a half of fitted value with respect to the volume fraction $f = 0.5$. Difference between the width of the air-gap r obtained from SEM ($r_{\mathrm{SEM}} = 63$ nm) and from the best-fit ($r_{\mathrm{fit}} = 78.68$ nm) comes from the fact, that the r estimated from SEM is a local value, but the value from the best-fit is obtained as a total response of the sample.

6.2. Analysis of the transverse magneto-optical response

Having confirmed the presence of the resonances in the fabricated magnetoplasmonic grating and successfully fitted realistic fabrication parameters to the measured Mueller spectra, the final step is to verify whether the TMOKE response of the structure is indeed enhanced as predicted [14]. For positive $(+M_T^{\mathrm{sat.}})$ and negative $(-M_T^{\mathrm{sat.}})$ orientations of the magnetic field two sets of 5 Mueller matrix spectra were measured and averaged in order to reduce noise. Since the experimental data on Fig. 11 clearly show block-diagonal shape [see Eq. (3)], we can directly calculate relative reflectivity R_p/R_s from Mueller matrix (3):

$$\frac{R_p}{R_s} = \frac{M_{11} + M_{12}}{M_{11} - M_{12}} = \frac{1 - \frac{M_{12}}{M_{11}}}{1 + \frac{M_{12}}{M_{11}}} = \frac{1+N}{1-N} \tag{11}$$

Figure 12 shows comparison between experimental ellipsometric data and model. Numerical data were calculated assuming the structure shown in Fig. 10 using the fitted parameters of Tab. 3. The left subplot shows very good matching between the relative reflectivity $R_p/R_s = 1+N/1-N$ calculated from experimental data (blue dots) and from numerical simulation (solid red lines). Moreover, calculated green line with the *s*-reflectivity R_s is expected to be quasi "featureless" while the p-reflectivity R_p should contain pronounced reflection dips linked to SPP excitations. The relative reflectivity R_p/R_s (which follows directly from the Mueller elements M_{12}) should therefore contain the signatures of the Fano resonances connected to the SPP excitations (and possibly also a Lorentzian FP slit resonance). The main surface plasmon polariton (SPP) peak at the wavelength $\lambda = 885$ nm is indeed observed and nicely fitted by the numerical model. Quite reasonable agreement was obtained in the region between 1.2 μm and 1.5 μm where the amplitude of interferences is reduced by the beam divergence.

The TMOKE response of the considered magnetoplasmonic structure can be experimentally easily characterized in an ellipsometric setup by measuring the absolute change of the relative reflectivity upon reversal of the external magnetic field [14]. This is obviously due to the fact that in transverse configuration the s-reflectivity will be unaffected by magnetization reversal:

$$\delta\frac{R_p}{R_s} = \frac{R_p}{R_s}\left(+M_T^{\mathrm{sat.}}\right) - \frac{R_p}{R_s}\left(-M_T^{\mathrm{sat.}}\right) \tag{12}$$

The right subplot of Fig. 12 shows comparison of the TMOKE response, Eq. (12). The MO response was calculated using the MO parameters of Bi:GIG estimated in Sec. 5 (Fig. 9). It can be clearly seen how TMOKE at first order gold/garnet SPP wavelength of 885 nm is resonantly enhanced. Moreover, other peaks are observed at the wavelengths 611 nm, 791 nm, and 1498 nm. The peaks at wavelength of 1498 nm, 885 nm, 791 nm, and 611 nm correspond to the excitation of the SPP by $+1^{\mathrm{st}}$, -1^{st}, -2^{nd}, and $+2^{\mathrm{nd}}$ diffracted orders, respectively. The order of SPP mode is defined by $m = \pm 1, \pm 2$ in 2.

It is striking how well the model reproduces over a very large spectral range both the relative reflectivity from Mueller matrix R_p/R_s and its difference $\delta R_p/R_s$. This once more underlines the accuracy of the described fitting procedure and the importance of taking into account all the described fabrication imperfections and measurement deviations such as angular spread.

#215021 - $15.00 USD Received 1 Jul 2014; revised 30 Jul 2014; accepted 30 Jul 2014; published 22 Aug 2014

Moreover this successful large scale fitting proves the correctness of the model used to design the magnetoplasmonic enhanced TMOKE grating. In future work it will be demonstrated how this model has been advantageously employed to demonstrate artificially engineering of the strength and the sign of the garnet's MO effect.

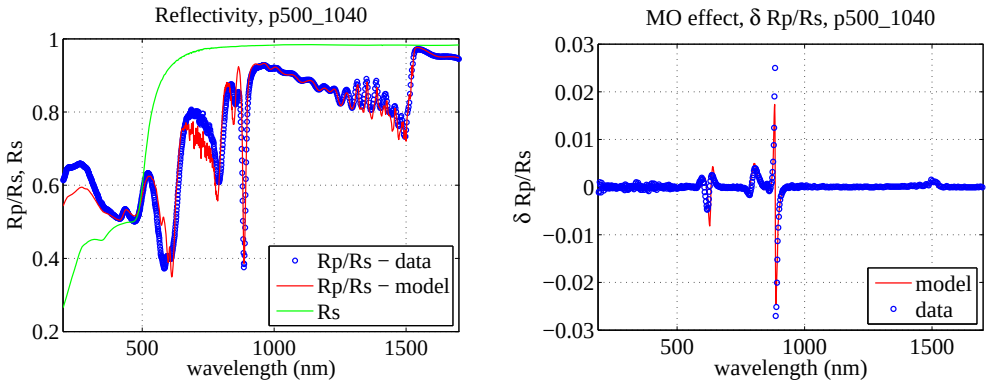

Fig. 12. Numerical and experimental data are compared. Left subplot shows good agreement of a calculated relative reflectivity with a model. Right subplot shows agreement between measured and calculated MO effect $\delta R_p/R_s = R_p/R_s(+M_T^{\mathrm{sat}}) - R_p/R_s(-M_T^{\mathrm{sat}})$.

7. Conclusions

In this paper we have demonstrated how Mueller matrix ellipsometry (extended with an in-plane magnetic circuit) combined with precise fitting can be used to analyze optical and magneto-optical spectra with sharp resonant features. The predicted enhancement of TMOKE near the SPP resonances of a gold-on-garnet grating have been perfectly fitted over a large spectral range by first determining the permittivity and gyrotropy dispersion of the constitutive garnet materials (sGGG and Bi:GIG) in the structure, and, most importantly, by taking into account a number of possible fabrication imperfections. Fitting of the experimental angular spread of the incidence Gaussian beam also contributed to this and allowed to explain the presence of interference fringes in the Mueller spectra. The described technique is a generic tool that can be used to study magneto-optic structures in many different configurations or geometries. This will be useful for the study of magnetoplasmonic structures providing enhancement of the MO effects due to interaction between resonant modes in the structure [14].

Acknowledgment

Partial support from the projects CZ.1.05/1.1.00/02.0070 (IT4Innovations), CZ.1.05/2.1.00/01.0040 (RMTVC), CZ.1.07/2.3.00/20.0074 (Nanobase), mobility project 7AMB14FR037, IRP 167/2014, and Czech Science Foundation 13-30397S is acknowledged.

#215021 - $15.00 USD Received 1 Jul 2014; revised 30 Jul 2014; accepted 30 Jul 2014; published 22 Aug 2014